







Cite this: *Chem. Commun.*, 2024, 60, 12868

Received 5th August 2024,
Accepted 3rd October 2024

DOI: 10.1039/d4cc03889d

rsc.li/chemcomm

Electrode–electrolyte interactions dictate thermal stability of sodium-ion batteries†

Susmita Sarkar, ^{‡ab} Avijit Karmakar, ^{‡a} Bairav S. Vishnugopi, ^a
Judith A. Jeevarajan ^c and Partha P. Mukherjee ^{*a}

This work delineates the thermal safety of full-scale sodium-ion batteries (SIBs) by interrogating the material-level electrochemical and thermal responses of micro and nano-structured tin (Sn) based anodes and sodium vanadium phosphate (NVP) cathodes in suitable electrolyte systems. Informed by these material-level signatures, we delineate cell-level thermal safety maps cognizant of underlying electrode–electrolyte interactions in SIBs.

Sodium-ion batteries (SIBs) have captured tremendous interest due to advantages such as the abundance and uniform distribution of sodium (Na) resources, low cost, and environmental friendliness.¹ While energy density, power density, and lifespan are key features for market integration, batteries used for electric vehicles and grid storage applications should also exhibit high thermal stability.² The cell-level thermal runaway (TR) is predominantly governed by choice of the electrode and electrolyte materials and the spatio-temporal evolution of different chemical interphases in the cell.³ In recent years, among the several cathode materials for SIBs, the NASICON-type sodium vanadium phosphate $\text{Na}_3\text{V}_2(\text{PO}_4)_3$ (NVP) has been extensively investigated due to its high ionic conductivity and theoretical energy density.⁴ Alloy-based materials such as silicon (Si), germanium (Ge), tin (Sn), and antimony (Sb), along with their binary and ternary alloys, show significant promise as anodes due to their high theoretical capacities and favorable electrochemical behavior, are applicable to SIBs.^{5–9} Amidst the wide range of candidate anodes, the development of Sn-based alloy-type anodes has garnered significant interest due to lower cost and environmental impact, and various aspects such as

their cycling stability, formation of solid electrolyte interphase (SEI), alloying/de-alloying induced structural degradation, and failure mechanism have been studied.^{10–12} Compared to commercially viable anode materials for SIBs, such as hard carbon and titanium-based materials, although Sn-based materials suffer from volume expansion, efforts are being made to overcome these challenges for future commercialization.^{13–15} While major research efforts have focused on demonstrating the electrochemical performance and overall lifespan of different cathode/anode couples, the thermal stability of SIBs has received relatively less attention.¹⁶

Various electrode/electrolyte interactions (*e.g.*, cathode/anode vs. carbonate/glyme),¹⁷ the growth of interphases,¹⁸ mechanical degradations (*e.g.*, cracking, deformation),¹⁹ and electrolyte additives can potentially affect the TR propensity. Importantly, while using Na metal in the system, the high chemical reactivity of Na can result in rapid electrolyte decomposition and the development of SEI,²⁰ necessitating the need for an electrolyte-specific assessment of thermal stability for SIBs. For instance, electrolyte additives such as fluoroethylene carbonate (FEC) added to electrolyte salts (*e.g.*, sodium perchlorate (NaClO_4)) in carbonate-based electrolytes (*e.g.*, ethylene carbonate (EC), propylene carbonate (PC), diethyl carbonate (DEC)) have been shown to stabilize the electrode/electrolyte interface for both cathode²¹ and anode,²² thus improving the cell longevity.²¹ However, the thermo-electrochemical interactions of FEC-based electrolytes with the cathode/anode materials and their implications on the overall thermal stability of sodium-ion cells are not fully understood.

In this study, we first examine the electrochemical response of micro(μ)- and nano(n)-Sn-based electrodes in $\text{NaClO}_4\text{:EC:PC:DEC}$ (base) and $\text{NaClO}_4\text{:EC:PC:DEC:FEC}$ (base + FEC) electrolytes (Fig. S1 of ESI†). The cell fabrication details are described in Section S1 of ESI.† The charge/discharge voltage response in Fig. 1a–d shows sequential stepwise plateaus for all the cases; however, for both the electrolytes, μ -Sn showed distinct plateaus compared to the n-Sn. μ -Sn in base electrolyte showed initial sodiation and desodiation capacity of ~ 855 and ~ 731 mA h g^{−1}

^a School of Mechanical Engineering, Purdue University, West Lafayette, Indiana 47907, USA. E-mail: pmukherjee@purdue.edu

^b Department of Mechanical and Aerospace Engineering, North Carolina State University, Raleigh, North Carolina 27695, USA

^c Electrochemical Safety Research Institute, UL Research Institutes, Houston, Texas 77204, USA

† Electronic supplementary information (ESI) available. See DOI: <https://doi.org/10.1039/d4cc03889d>

[‡] S. S. and A. K. share equal contribution.



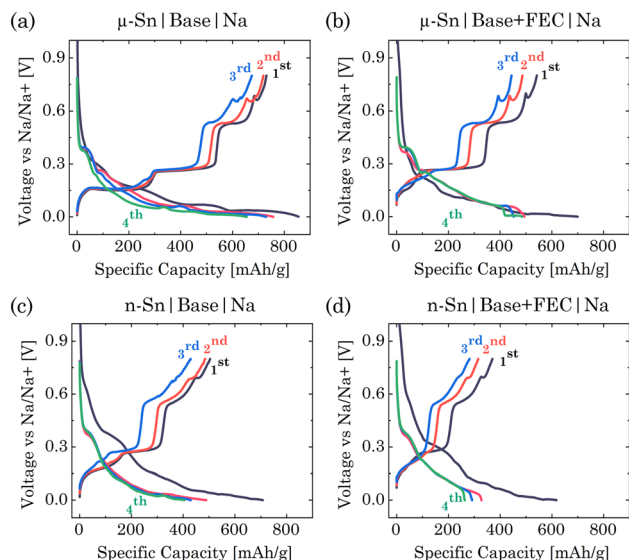


Fig. 1 Voltage profile of μ -Sn based half-cell using the electrolytes of (a) EC:PC:DEC-base, (b) EC:PC:DEC:FEC-base + FEC, and n-Sn-based half-cell using the electrolytes of (c) EC:PC:DEC-base, (d) EC:PC:DEC:FEC-base + FEC.

with a coulombic efficiency of 85.49%. The 2nd and 4th sodiation cycles show a capacity of ~ 757 and ~ 674 mA h g⁻¹, indicating a significant capacity loss of around 11% from the 2nd sodiation. When μ -Sn was dipped in the FEC-based electrolyte, although the 1st sodiation (~ 700 mA h g⁻¹) and desodiation (~ 542 mA h g⁻¹) capacity were slightly lower than the previous case, the capacity retention from 2nd to 4th discharge significantly improved (~ 494 mA h g⁻¹ to ~ 484 mA h g⁻¹, loss around 2%). The coulombic efficiency was around 77.42%, caused by the formation of NaF-like SEI components under FEC decomposition.²³ With the n-Sn in the base electrolyte, 1st sodiation/desodiation capacity was $\sim 708/504$ mA h g⁻¹, indicating a coulombic efficiency of 71.18%. The loss from the 2nd to 4th sodiation cycle for n-Sn in the base electrolyte was around 12.09% (488 to 429 mA h g⁻¹). The n-Sn in FEC containing electrolyte showed 1st sodiation/desodiation capacity around 617 and 370 mA h g⁻¹. The coulombic efficiency for this system was approximately 60%, indicating the lowest efficiency observed in the 1st cycle compared to all other cases. The capacity during the 2nd to 4th sodiation cycles for n-Sn in an FEC environment decreases from 328 mA h g⁻¹ to 281 mA h g⁻¹, resulting in a loss of approximately 14.33%. Overall, the sodiation/desodiation capacity in the 1st cycle was decreased for n-Sn primarily due to its increased reactivity under the higher surface area and agglomeration effects hindering electrical contact,^{24,25} and with the addition of FEC, it was further reduced. FEC is known to form a resistive interphase that limits the charge transfer kinetics and inhibits the formation of some intermediated phases, resulting in a lower capacity for SIB anodes.¹²

After the cycling of Sn-based half cells, their thermal stability analyses were performed using an accelerating rate calorimetry (ARC) following the heat-wait-see (HWS) method (parameters listed in Table S1 of ESI†). Fig. 2a and b show the ARC temperature response of half cells with μ -Sn and n-Sn in base and base + FEC electrolytes. The TR characteristics

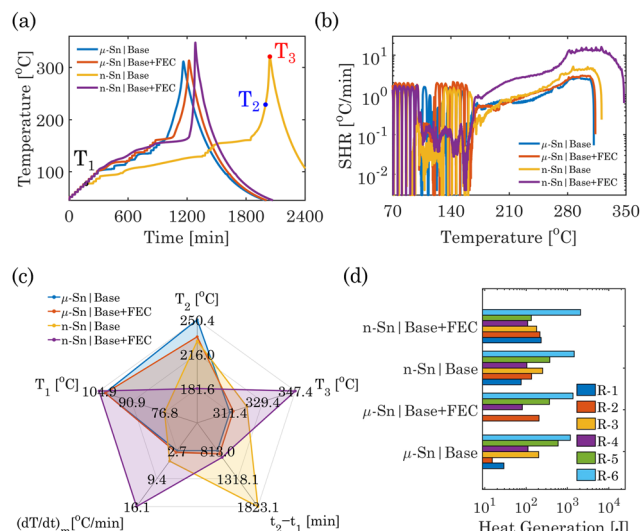


Fig. 2 The ARC experiments to probe the thermal stability of the Sn electrode. (a) Temperature response of μ -Sn and n-Sn-based half-cell using the electrolytes—base and base + FEC. (b) The temperature increase and the corresponding self-heating rates (SHR) for all the cases. (c) Thermal safety characteristics and (d) comparison of heat generation of the μ and n-Sn cases in two different electrolytes.

temperatures are defined in Table S2 of ESI†. The μ -Sn in the base electrolyte half-cell shows $T_1 = 102.39$ °C and $T_2 = 250.38$ °C; beyond that, it reaches $T_3 = 311.38$ °C at a significantly higher heating rate (up to 2.69 °C min⁻¹). While FEC was added to the base electrolyte, μ -Sn showed almost slightly higher $T_1 = 102.21$ °C and $T_3 = 313.27$ °C; however, T_2 decreased to 233.41 °C. When n-Sn was used in the base electrolyte, both $T_1 = 91.85$ °C and $T_2 = 229.06$ °C were reduced compared to the μ -Sn in the base electrolyte. The T_3 for n-Sn in the base electrolyte increases to 320.76 °C. With the incorporation of FEC in the base electrolyte, T_1 increases significantly to 104.81 °C, and T_2 decreases significantly to 181.55 °C. The addition of FEC significantly contributes to stabilizing the interface of n-Sn with a larger high reactive surface area, leading to higher self-heating onset; however, as soon as the SEI decomposes, it goes to TR rapidly. A significantly higher self-heating rate (up to 16.08 °C min⁻¹) is detected, which results in TR and a substantially larger $T_3 = 347.73$ °C, corresponding to the thermal decomposition of the interphases and the reaction with molten Na. The spider charts in Fig. 2c provide a comprehensive overview of the essential thermal safety characteristics exhibited by the four Sn|Na systems in different electrolytes.

In between T_1 and T_3 , the ARC thermal response of the Sn-half cells can be segmented into six distinct zones based on the change law in the temperature rate corresponding to specific reaction mechanisms.²⁶ The description of these different zones and their start and end temperatures are summarized in Fig. S5 and Table S3 of ESI†. Fig. 2d compares the generated heat in the μ and n-Sn in base and base + FEC electrolytes due to six significant reactions (R-1 to R-6). The total amount of heat generated for n-Sn in base (2400.6 J) and n-Sn in base + FEC



(2933.3 J) cases was relatively higher than that of μ -Sn in base (2116.7 J) and μ -Sn in base + FEC (2032.4 J) cases. All six exotherms were distinctly identified for the Sn-based half cells in different electrolytes except for μ -Sn in the base + FEC electrolyte. The R-1 and R-2 reactions were merged for μ -Sn in the base + FEC electrolyte, and the net heat generation is higher compared to the sum of the heat generation from R-1 + R-2 in the base electrolyte half-cell. The heat generation from R-3 was also extremely small for the μ -Sn in the base + FEC electrolyte compared to the base electrolyte, suggesting minor interaction between molten Na and electrolyte containing FEC. Incorporating FEC significantly reduces both the heat generation from the SEI decomposition of Sn (R-4) and Sn metal-electrolyte (R-5) interactions for μ -Sn. Moreover, the heat generated from R-6 is comparatively higher for μ -Sn in FEC-electrolyte. Interestingly, we have noticed that the particle size of Sn also affects the amount of generated heat due to the decomposed SEI-Na reaction. The n-Sn in the base electrolyte displayed significantly higher heat generation from R-1 and R-2 compared to the μ -Sn and is primarily caused by the larger high reactive surface area in the nanoparticle. The addition of FEC to n-Sn further increased the amount of R-1 and R-2. The R-3 reaction produced slightly lower heat for n-Sn in the base + FEC electrolyte than the base electrolyte. This could be attributed mainly to the fact that a considerable amount of electrolyte has been consumed by n-Sn to produce the SEI layer with a larger surface area, thus reducing the total amount of available electrolyte to react with Na. Compared with μ -Sn, a slightly lower heat generation for n-Sn in the base electrolyte for the R-4 reaction can be observed. The heat produced for R-5 in the n-Sn case shows a similar trend as μ -Sn; FEC reduces the heat generation for the n-Sn-electrolyte reaction. Compared to μ -Sn, the net heat generation from R-4 and R-5 has significantly decreased for n-Sn in FEC electrolytes, which can be attributed to parasitic reactions primarily related to a higher amount of SEI growth under an increased nanoparticle surface area.²⁷ Finally, R-6 for n-Sn in FEC showed higher heat generation than the base electrolyte, similar to the trend observed for the μ -Sn case.

To further understand the electrochemical and thermal stability, X-ray photoelectron spectroscopy (XPS) analysis can provide insights into the different compounds formed in the SEI layer of the Sn-based half cells (Fig. S2 of ESI†).²⁸ Fig. 3a and b show the normalized percentage of each bond in the carbon (C) and oxygen (O) elements for all cases. The addition of FEC to the base electrolyte forms a thermally protective layer on the Sn-based electrode surface, thus reducing the amount of heat generated from the R-4 and R-5 reactions under the same surface area. The interphase composition of Sn-based electrodes cycled in FEC-based electrolyte has smaller peak intensities corresponding to organic compounds and intense sodium fluoride (NaF) peak, suggesting that the formation of inorganic NaF suppresses the formation of organic species such as carbonates (Na_2CO_3), esters ($\text{O}=\text{C}-\text{OR}$), and ethers ($\text{C}-\text{O}-\text{C}$), *etc.* on the Sn surface and reduces the amount of heat generation. Conversely, the heat generated from R-6 is significantly

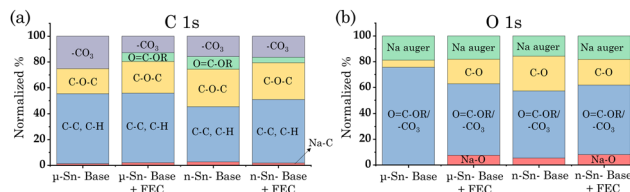


Fig. 3 Normalized percentage of (a) C 1s and (b) O 1s with different electrode and electrolyte combinations, as obtained by analyzing the XPS data.

higher in FEC-electrolyte for Sn-based half cells. In the presence of NaClO_4 , the interphase composition for the Sn-based electrodes shows considerable CO evolution due to the decarbonylation process, suggesting a significantly higher decomposition of FEC and larger heat generation compared to the base electrolyte.²⁹ The manifestation of such an exotherm in the thermal stability of Sn-based half-cells in FEC-containing electrolytes highlights the underpinning correlation between the interphase interaction and thermal stability.

It is essential to understand the overall cell-level thermal stability of a SIB. In the previous section, the μ -Sn in the base + FEC electrolyte depicted the least heat generation under the ARC thermal response; henceforth, it was chosen as the anode material to construct the SIB full-cell. A suitable material with high capacity and the slightest structural changes during sodiation and desodiation is desired as the positive electrode material. NVP is a highly researched cathode due to its high ionic transportation, theoretical capacity (118 mA h g^{-1}),³⁰ and excellent thermal stability at temperatures up to 450°C .³¹ The electrochemical and thermal response of fabricated NVP-based half-cell with counter electrode Na metal in base + FEC electrolyte is provided in Fig. S3 of ESI†. The thermal signature of NVP-half cells can be segmented into distinct reaction zones as Sn-based half cells, depicting the NVP-electrolyte interaction and electrolyte decomposition. The thermal signatures of the μ -Sn and NVP-based half-cells can be used to extract the thermo-kinetic parameters of the individual μ -Sn and NVP electrodes in base + FEC electrolyte.²⁶ Further description of the kinetic parameter extraction from the ARC profiles is presented in Section S2.1 and Fig. S6 and S7 in ESI†; the kinetic parameters of the exothermic reaction for μ -Sn and NVP electrodes in base + FEC electrolyte are summarized in Tables S4 and S5 (ESI†). This information can be further utilized to develop the computational model capturing the cell-level thermal stability of SIB based on the observed material-level response. The electrochemical and thermal response of fabricated SIB full-cell based on the NVP cathode and Sn anode electrodes in base + FEC electrolyte is provided in Fig. S4 of ESI†. The kinetics of the material thermal reactions are combined to simulate the cell-level ARC behavior of μ -Sn|base + FEC|NVP full-cell, as shown in Section S2.2 of ESI†. The simulated temperatures and temperature rates fit well with the experimental results (Fig. S8 of ESI†). The thermal model developed based on material thermal analysis and detailed reaction kinetics can reasonably predict the TR behaviors of full-scale SIBs.



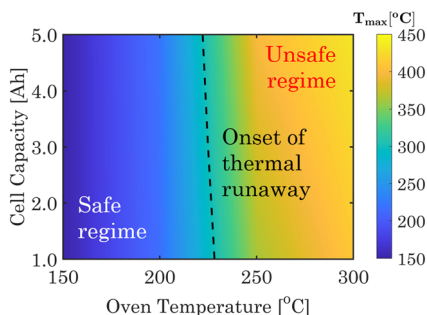


Fig. 4 Thermal safety phase map for the NVP- μ -Sn-based SIBS under different capacity and oven temperatures. The black line represents the initiation of thermal runaway under oven conditions.

Using the developed cell-level TR heat generation model, standard oven tests are initially conducted on 1 A h full-cell in pouch format comprising μ -Sn|base + FEC|NVP. Section S2.3, Table S6, and Fig. S9 of ESI[†] provide details about the cell-level oven test model. The thermal safety maps in Fig. 4 display the maximum cell temperature observed during thermal abuse scenarios, considering different capacities (1–5 A h) and oven temperatures (150–300 °C). The phase map first identifies a safe zone where the cell exhibits a stable temperature without experiencing an exponential rise, even within the designated operating oven temperature. Then, the critical oven temperature for a TR is displayed, which ranges from 220 to 230 °C, depending on the pouch cell capacity. Once the critical value is surpassed, the cell undergoes a rapid and exponential temperature increase, resulting in potential safety incidents marked as unsafe regimes. The experimentally informed virtual TR analytics platforms can help prevent cell-to-cell failures in SIB modules.

In summary, this study delineates the role of electrolytes in modulating the thermal safety of full-scale SIBs by interrogating the material-level electrochemical and thermal responses of μ and n-structured Sn-based anodes and NVP cathodes in different electrolytes. The ARC experiments identified that n-Sn produced more exothermic heat than μ -Sn under electrolytes without FEC additives. The nanoparticles in n-Sn have a higher surface area, thereby increasing their reactivity towards the electrolyte to produce more SEI products and intense heat release. On adding FEC to the electrolyte, the heat generation for μ -Sn decreased further as the formation of inorganic NaF suppresses the formation of organic species on the Sn surface. Informed by these material-level signatures, we developed a computational model to capture the cell-level thermal stability of SIBs comprising Sn-based anodes and NVP cathodes in FEC-containing electrolytes. Our analysis delineates thermal safety maps for SIBs based on simulated oven test signatures that could prove decisive in deconvolving the innate thermal instability signatures of electrode–electrolyte pairs in SIB chemistry. Building on the current study, future research directions have been described in ESI[†].

The funding for this research was provided by UL Research Institutes through the Center for Advances in Resilient Energy Storage (CARES).

Data availability

The data supporting this article have been included as part of ESI[†].

Conflicts of interest

There are no conflicts to declare.

Notes and references

- Y. Tian, G. Zeng, A. Rutt, T. Shi, H. Kim, J. Wang, J. Koettgen, Y. Sun, B. Ouyang, T. Chen, Z. Lun, Z. Rong, K. Persson and G. Ceder, *Chem. Rev.*, 2021, **121**, 1623–1669.
- C. Yang, S. Xin, L. Mai and Y. You, *Adv. Energy Mater.*, 2021, **11**, 2000974.
- B. S. Vishnugopi, M. T. Hasan, H. Zhou and P. P. Mukherjee, *ACS Energy Lett.*, 2022, **8**, 398–407.
- R. R. Samigullin, O. A. Drozhzhin and E. V. Antipov, *ACS Appl. Energy Mater.*, 2021, **5**, 14–19.
- Y. Jin, Y. Tan, X. Hu, B. Zhu, Q. Zheng, Z. Zhang, G. Zhu, Q. Yu, Z. Jin and J. Zhu, *ACS Appl. Mater. Interfaces*, 2017, **9**, 15388–15393.
- F. S. Ke, K. Mishra, L. Jamison, X. X. Peng, S. G. Ma, L. Huang, S. G. Sun and X. D. Zhou, *Chem. Commun.*, 2014, **50**, 3713–3715.
- Z. Lin, X. Liu, X. Xiong, S. Wei, W. Liu and Z. Lin, *Chem. Commun.*, 2020, **56**, 10187–10190.
- L. Sun, Y. Liu, L. J. Wang and Z. Jin, *Adv. Funct. Mater.*, 2024, **34**(39), 2403032.
- M. M. Zhang, K. Shen, M. Y. Gao, X. M. Guo, J. H. Zhang, H. X. Gu, Q. H. Kong and Z. Jin, *Batteries Supercaps*, 2024, **7**(9), e202400139.
- J. Zhang, J. Gai, K. Song and W. Chen, *Cell Rep. Phys. Sci.*, 2022, **3**(5), 100868.
- S. Sarkar, H. J. Gonzalez-Malabet, M. Flannagin, A. L'Antigua, P. D. Shevchenko, G. J. Nelson and P. P. Mukherjee, *ACS Appl. Mater. Interfaces*, 2022, **14**, 29711–29721.
- S. Sarkar and P. P. Mukherjee, *Energy Storage Mater.*, 2021, **43**, 305–316.
- X. Wu, X. Lan, R. Hu, Y. Yao, Y. Yu and M. Zhu, *Adv. Mater.*, 2022, **34**, e2106895.
- F. Xin and M. S. Whittingham, *Electrochem. Energy Rev.*, 2020, **3**, 643–655.
- B. Qin, A. Schiele, Z. Jusys, A. Mariani, T. Diemant, X. Liu, T. Brezesinski, R. J. Behm, A. Varzi and S. Passerini, *ACS Appl. Mater. Interfaces*, 2020, **12**, 3697–3708.
- C. Delmas, *Adv. Energy Mater.*, 2018, **8**, 1703137.
- K. Du, A. Rudola and P. Balaya, *ACS Appl. Mater. Interfaces*, 2021, **13**, 11732–11740.
- J. Wu, S. Weng, X. Zhang, W. Sun, W. Wu, Q. Wang, X. Yu, L. Chen, Z. Wang and X. Wang, *Small*, 2023, **19**, e2208239.
- B. Liu, Y. Jia, C. Yuan, L. Wang, X. Gao, S. Yin and J. Xu, *Energy Storage Mater.*, 2020, **24**, 85–112.
- L. Gao, J. Chen, Q. Chen and X. Kong, *Sci. Adv.*, 2022, **8**, eabm4606.
- A. Nimkar, N. Shpigel, F. Malchik, S. Bublil, T. Fan, T. R. Penki, M. N. Tsubery and D. Aurbach, *ACS Appl. Mater. Interfaces*, 2021, **13**, 46478–46487.
- J. Fondard, E. Irisarri, C. Courrèges, M. R. Palacin, A. Ponrouch and R. Dedryvère, *J. Electrochem. Soc.*, 2020, **167**, 070526.
- J. Y. Jang, Y. Lee, Y. Kim, J. Lee, S.-M. Lee, K. T. Lee and N.-S. Choi, *J. Mater. Chem. A*, 2015, **3**, 8332–8338.
- M. Gyanprakash and C. K. Rastogi, *J. Electroanal. Chem.*, 2023, **931**, 117176.
- Y. Gao, L. Fan, R. Zhou, X. Du, Z. Jiao and B. Zhang, *Nano-Micro Lett.*, 2023, **15**, 222.
- A. Karmakar, H. W. Zhou, B. S. Vishnugopi, J. A. Jeevarajan and P. P. Mukherjee, *J. Electrochem. Soc.*, 2024, **171**(1), 010529.
- D. J. Arnot, E. Allcorn and K. L. Harrison, *J. Electrochem. Soc.*, 2021, **168**, 110509.
- L. Wu, H. Fu, W. Lyu, L. Cha, A. M. Rao, K. Guo, J. Zhou, S. Wen and B. Lu, *ACS Nano*, 2024, **18**, 13415–13427.
- G. M. Hobold, A. Khurram and B. M. Gallant, *Chem. Mater.*, 2020, **32**, 2341–2352.
- J. Xiao, X. Li, K. Tang, D. Wang, M. Long, H. Gao, W. Chen, C. Liu, H. Liu and G. Wang, *Mater. Chem. Front.*, 2021, **5**, 3735–3764.
- S. Y. Lim, H. Kim, R. A. Shakoar, Y. Jung and J. W. Choi, *J. Electrochem. Soc.*, 2012, **159**, A1393–A1397.

